Electronic Supplementary Material (ESI) for Journal of Materials Chemistry A.
This journal is © The Royal Society of Chemistry 2021

Supporting Information

Facile synthesis of antimony-doped Cu/Cu_2O catalyst with robust CO production in broad potentials for CO_2 electrochemical reduction

Hongyu Chen,‡[a] Zhaojie Wang,‡[b] Shoufu Cao,[b] Siyuan Liu,[b] Xiaojing Lin,[b] Yi Zhang,[b] Yizhu Shang,[b] Qiuying Zhu,[b] Sainan Zhou,[b] Shuxian Wei,[a] Baojun Wei,*[a] Daofeng Sun,[b] Xiaoqing Lu*[b]

[a]College of Science, China University of Petroleum, No.66 Changjiang West road, Huangdao District, Qingdao, Shandong 266580, P. R. China

[b]School of Materials Science and Engineering, China University of Petroleum, No.66 Changjiang West road, Huangdao District, Qingdao, Shandong 266580, P. R. China

Corresponding Author:

*E-mail: weibj@upc.edu.cn; luxq@upc.edu.cn

‡These authors contributed equally to this work

Keywords: carbon dioxide reduction, antimony doped Cu/Cu_2O, high selectivity, DFT calculation, *CO pre-adsorption

Number of pages: 29

Computational detail

The calculations were performed by spin-polarized density functional theory (DFT) as accomplished in Vienna Ab initio Simulation Package (VASP) 6.1.0 with Perdew-Burke-Ernzerhof (PBE) generalized gradient approximation (GGA).[S1,S2] The cutoff energy was set as 420 eV after cutoff testing and the k-points were set to be 3 × 3 × 1 and 11 × 11 × 1 for all the geometric and electronic structures optimization, respectively. The electronic energy and forces were converged to within 10^{-5} eV and 0.02 eV/Å, respectively. The method of the Grimme (DFT+D3) was considered for the van der Waals interactions. The VASP implicit solvent model was used to consider the effect of water.[S3]

Changes of Gibbs free energy were calculated by the computational hydrogen electrode (CHE) model, in which the reaction: $H^+(aq) + e^- = 1/2\ H_2(g)$ is equilibrated at 0 V vs the reversible hydrogen electrode (RHE) at 101325Pa.[S4] The change of Gibbs free energy (ΔG) for each elementary step was defined as follows,

$$\Delta G = \Delta E + \Delta E_{ZPE} - T\Delta S + \Delta G_U + \Delta G_{pH}$$

where ΔE is the reaction energy, ΔE_{ZPE} and ΔS are the zero-point energy (ZPE) and the entropy difference between the products and the reactants at room temperature (T = 298.15 K), respectively. They were all calculated based on vibration analysis with standard methods. For the vibration analysis of intermediate states, frequencies were calculated by treating all 3N degrees of the adsorbates as vibrational in the harmonic oscillator approximation, and any changes in the vibrations of the substrate surface were assumed as the minimal. For fugacity of gaseous species (CO_2, CO, and H_2), the

standard state pressure of 101325 Pa was used. ΔG_U is the contribution of the applied electrode potential (U) to ΔG, and here is set as 0 V. The ΔG_{pH} represents the free energy contribution due to the variations in H concentration, and in this work the contribution of pH was excluded from consideration.

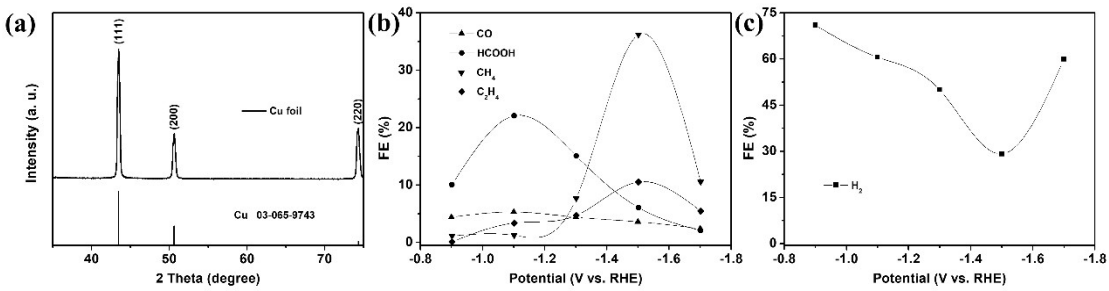

Figure S1. (a) XRD pattern of commercial Cu foil, (b-c) Faradaic efficiency of all products on Cu foil at each potential.

Cu foil (0.127 mm thick, annealed, 99.9%) was purchased from Alfa Aesar Company. To prepare the electrode, the Cu foil was placed in a solution containing CH_3COCH_3, C_2H_5OH, and 2 M HCl for ultrasonic treatment, and then washed by deionized water for several times and dried under vacuum at 60 °C.

In order to confirm the reliability of our experimental reaction system, we chose Cu foil as control for performance evaluation. XRD pattern of Cu foil is illustrated in Figure S1a. Three diffraction peaks at 43.49°, 50.64°, and 74.35° correspond to the (111), (200), and (220) planes of Cu (JCPDS 03-065-9743), respectively. The product distribution of Cu foil is illustrated in Figure S1b and S1c. As shown in Figure S1b, HCOOH and CO are the main reduction products at low potential, in which the FE of HCOOH reaches 22% of the maximum at -1.1 V. With the negative shift of working potential, the FE of HCOOH and CO decreases gradually, while that of CH_4 and C_2H_4 increases and reaches the maximum of 36.1% and 10.5% at -1.5 V, respectively. Meanwhile, the FE of H_2 (Figure S1c) is higher than 30%, and decreases with the increase of hydrocarbons at high potential. As reported by Hori et al.[S5], HCOOH and CO are dominant in their experiment at low potential, while CH_4 and C_2H_4 at high potential. Meanwhile, with the negative shift of electrode potential, the FE of H_2

gradually decreases. The similar product distribution and trend is achieved in our experiments. Moreover, the main product in Hori's experiment is CH_4, which is confirmed in our experiment as well. All the results suggest the reliability of the potential and products in our experiments.

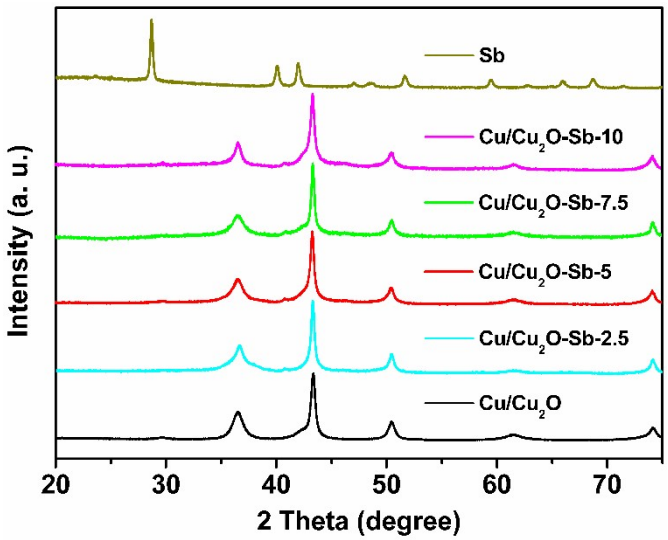

Figure S2. XRD patterns of Cu/Cu_2O, Cu/Cu_2O-Sb-2.5, Cu/Cu_2O-Sb-5, Cu/Cu_2O-Sb-7.5, Cu/Cu_2O-Sb-10 and pristine Sb.

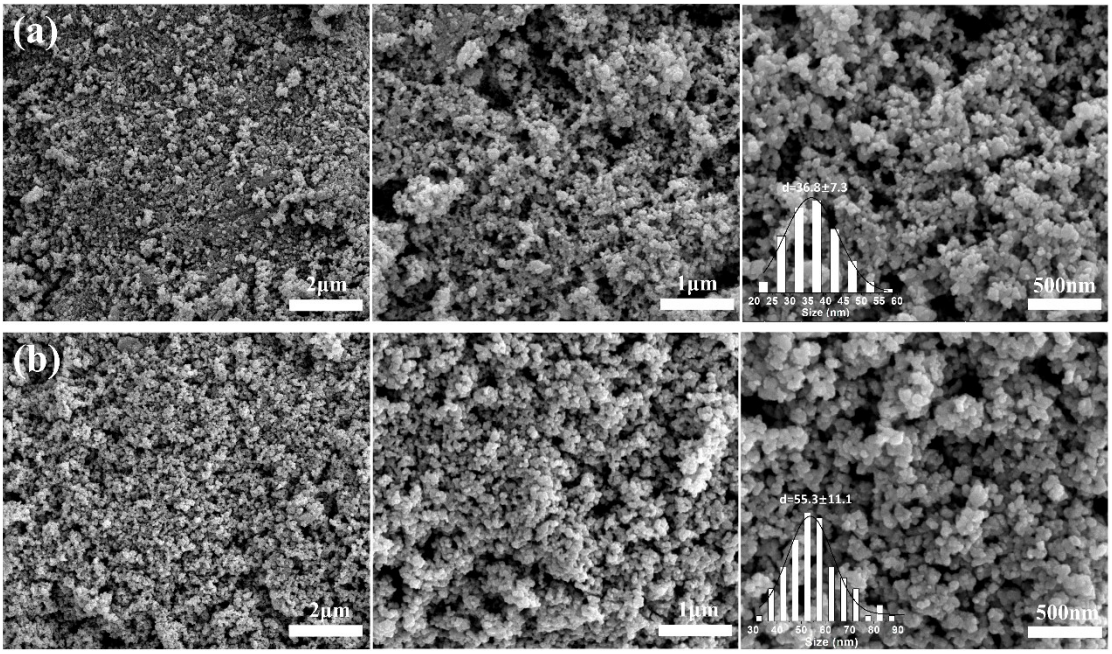

Figure S3. Low- and high-magnification SEM image and the size distribution histogram (inset) of (a) Cu/Cu_2O-Sb-5 and (b) Cu/Cu_2O.

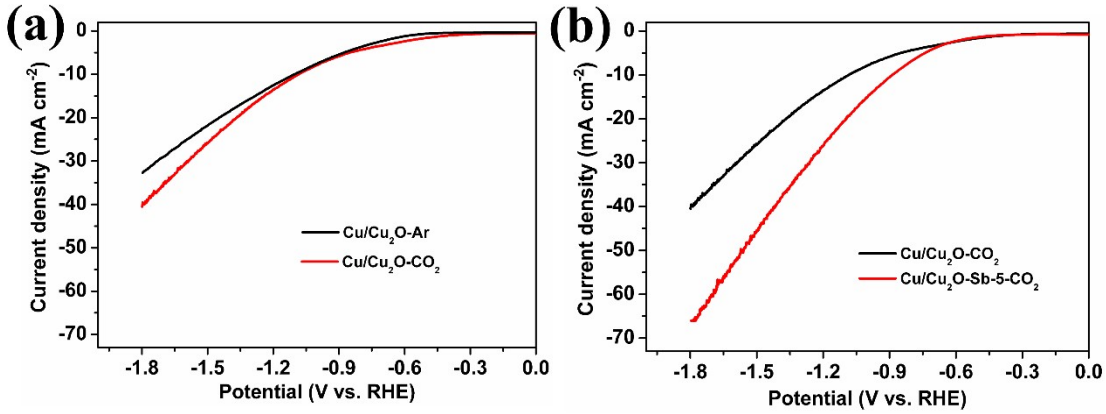

Figure S4. LSV curves of Cu/Cu_2O measured in Ar- and CO_2-saturated electrolyte, Cu/Cu_2O-Sb-5 and Cu/Cu_2O in CO_2-saturated electrolyte at a scan rate of 5 mV s^{-1}.

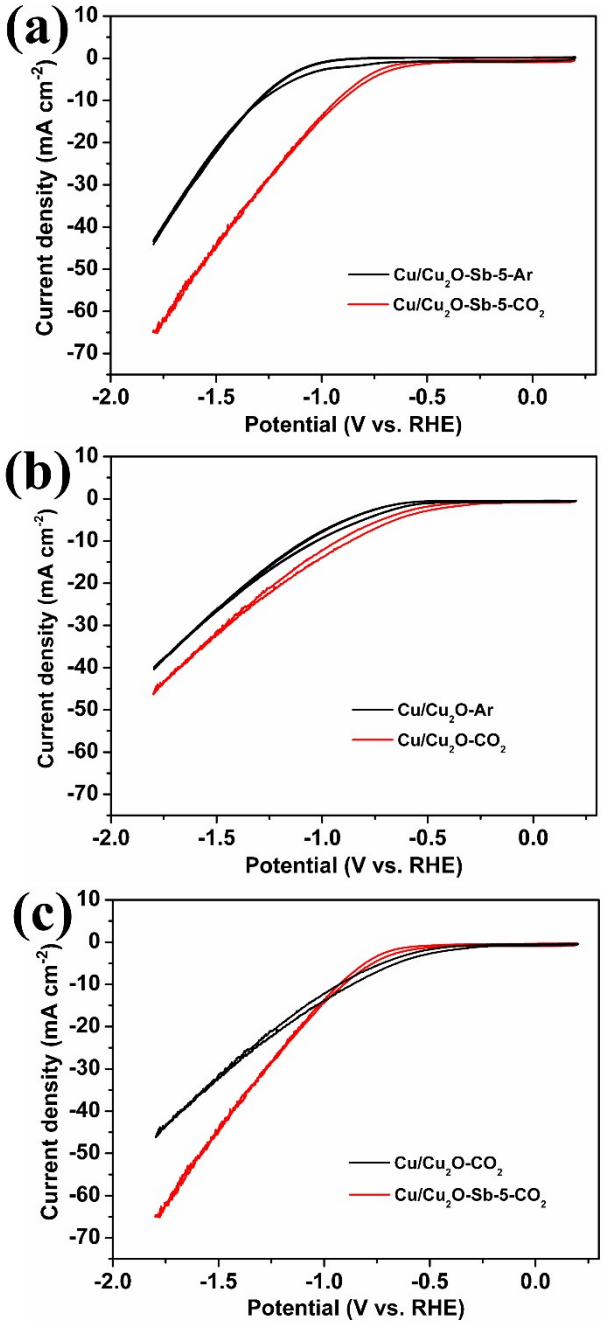

Figure S5. Cyclic voltammograms of (a) Cu/Cu_2O-Sb-5 in Ar- and CO_2-saturated electrolyte, (b) Cu/Cu_2O in Ar- and CO_2-saturated electrolyte, (c) Cu/Cu_2O-Sb-5 and Cu/Cu_2O in CO_2-saturated electrolyte at a scan rate of 20 mV s^{-1}.

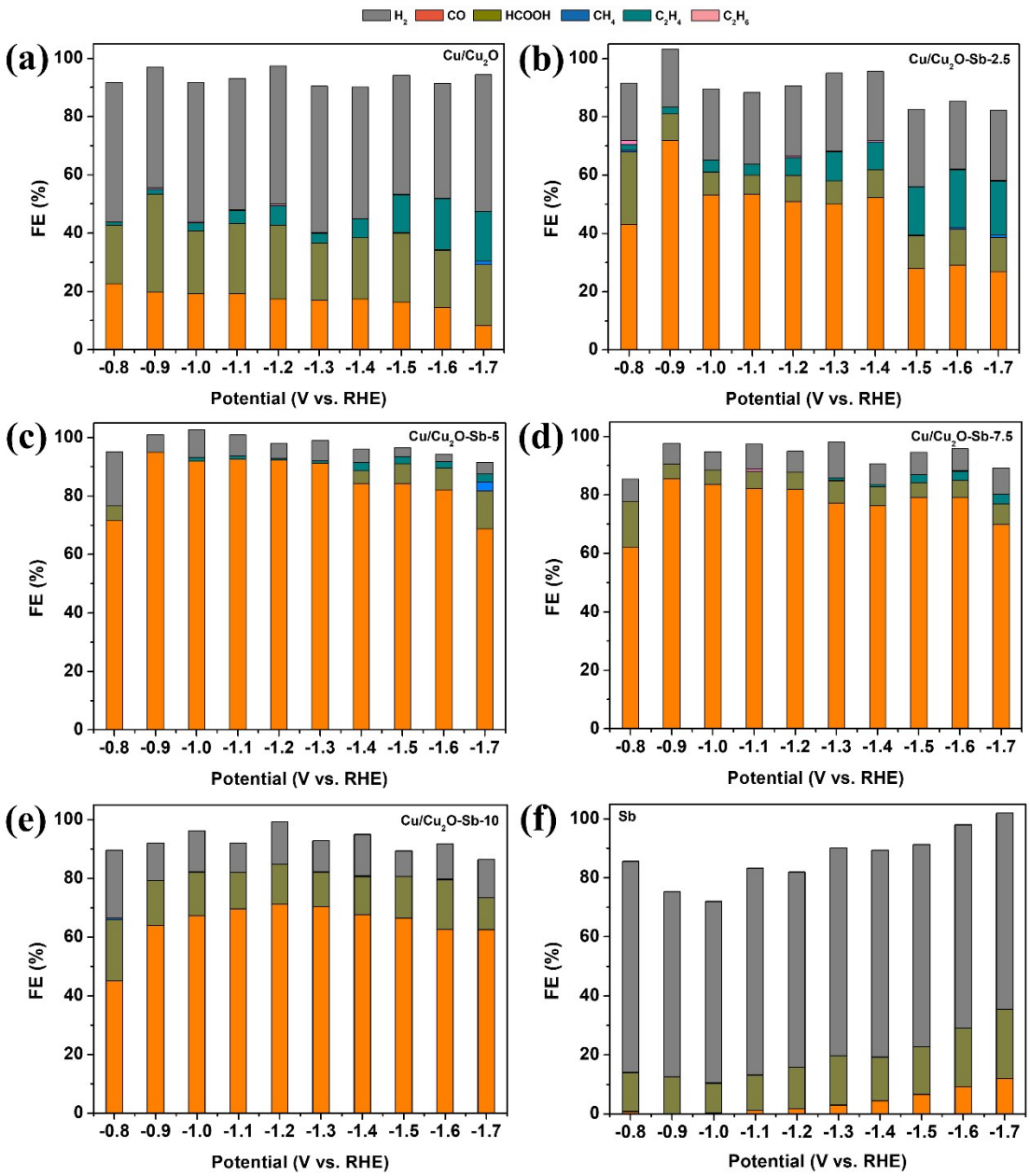

Figure S6. Faradaic efficiency of all products on as-prepared catalysts at each potential, respectively. (a) Cu/Cu_2O, (b) Cu/Cu_2O-Sb-2.5, (c) Cu/Cu_2O-Sb-5, (d) Cu/Cu_2O-Sb-7.5, (e) Cu/Cu_2O-Sb-10, (f) Sb.

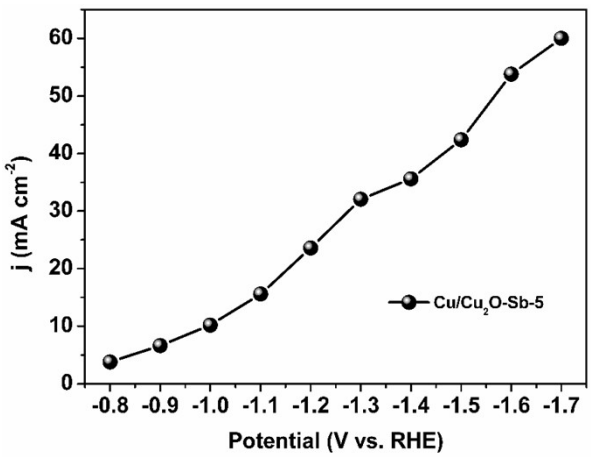

Figure S7. The total current density of Cu/Cu_2O-Sb-5 catalyst from -0.8 V to -1.7 V.

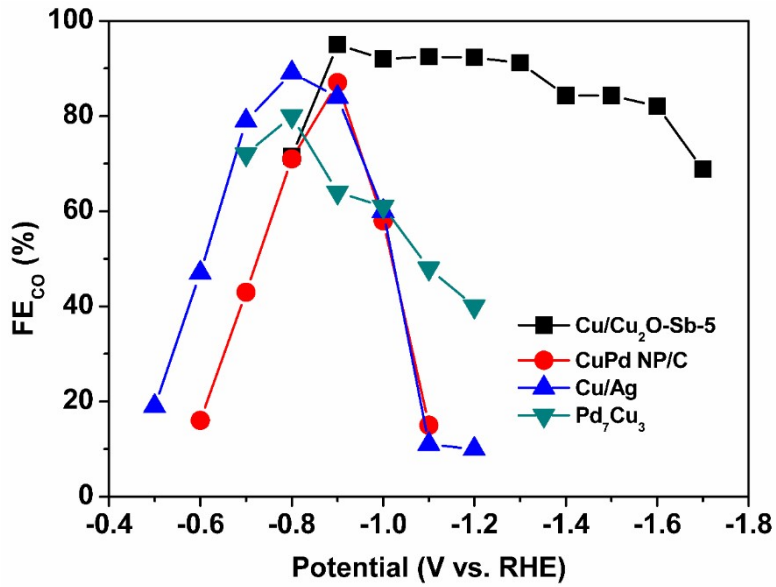

Figure S8. Comparison of the CO selectivity of our Cu/Cu_2O-Sb-5 with some previous Cu-based noble metal catalysts (CuPd NP/C,[S6] Cu/Ag,[S7] Pd_7Cu_3.[S8])

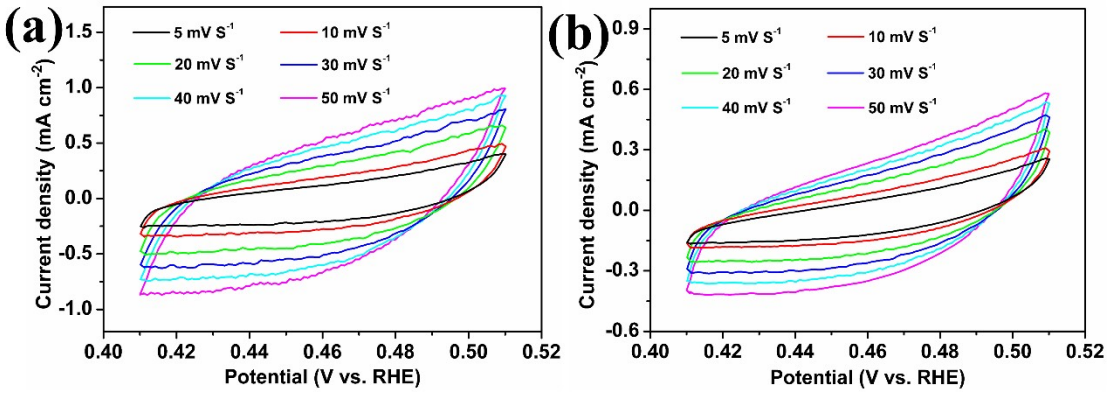

Figure S9. Electrochemical surface area measurement. Cyclic voltammetry scans on (a) Cu/Cu_2O-Sb-5, (b) Cu/Cu_2O between 0.41 and 0.51 V in CO_2-saturated 0.1 M $KHCO_3$ solution at scan rates of 5, 10, 20, 30, 40, and 50 mV s^{-1}.

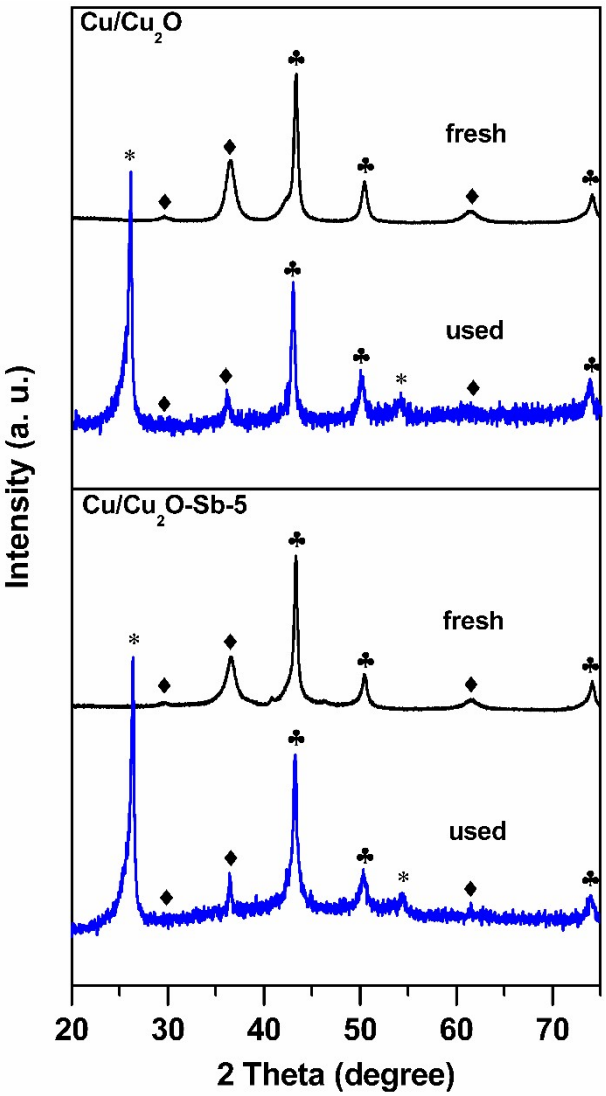

Figure S10. XRD patterns of fresh and used (i.e., after 10 h CO_2 reduction electrolysis) Cu/Cu_2O and Cu/Cu_2O-Sb-5 catalysts. Cu and Cu_2O are marked with ♣ and ♦. Reflections from the carbon paper used as substrate are marked with *.

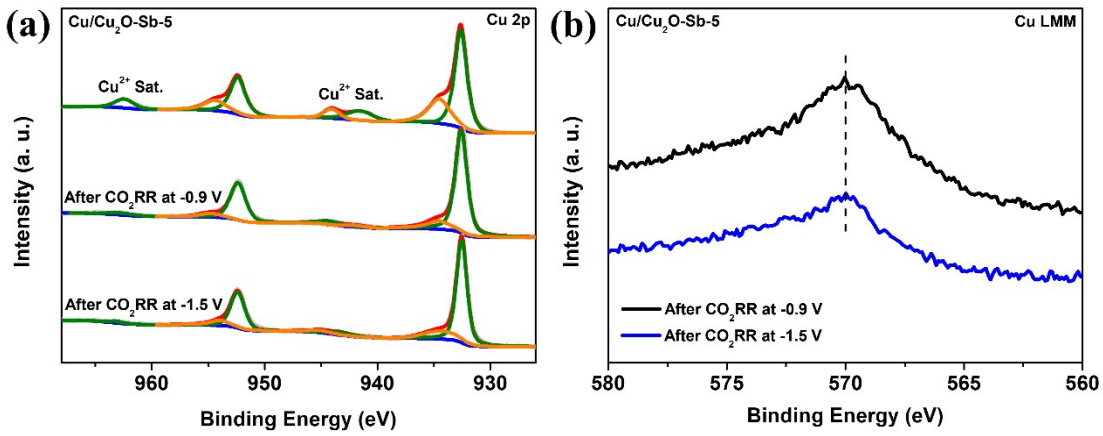

Figure S11. (a) Cu 2p XPS and (b) Cu LMM Auger spectra of Cu/Cu_2O-Sb-5 after CO_2RR at different potentials.

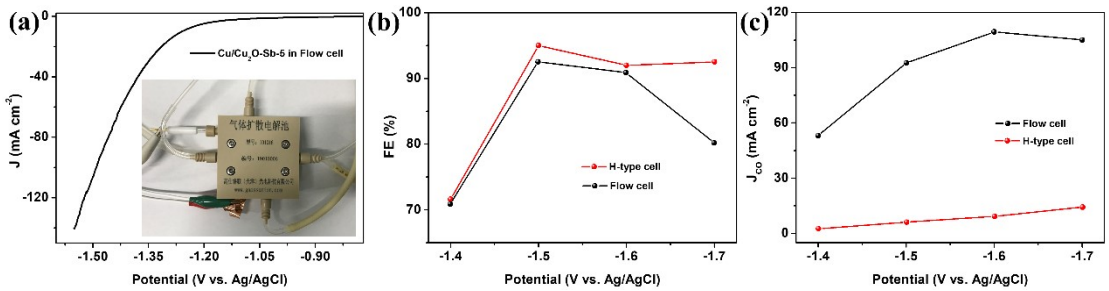

Figure S12. (a) LSV curve of Cu/Cu_2O-Sb-5 in flow cell at a scan rate of 5 mV s^{-1}. FE (b) and partial current density (c) of CO for Cu/Cu_2O-Sb-5 in H-type cell and flow cell. (A flow cell equipped with GDE device was applied for CO_2RR. A commercial Pt electrode was used as anode and an Ag/AgCl was acted as the reference electrode. 1 M KOH aqueous solution was utilized as electrolyte, which were separated by a piece of anion-exchange membrane.)

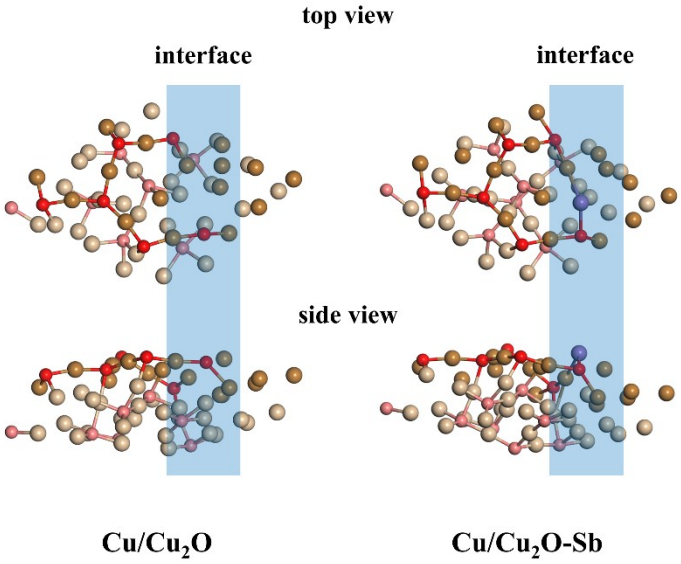

Figure S13. Optimized structures of Cu/Cu_2O and Cu/Cu_2O-Sb.

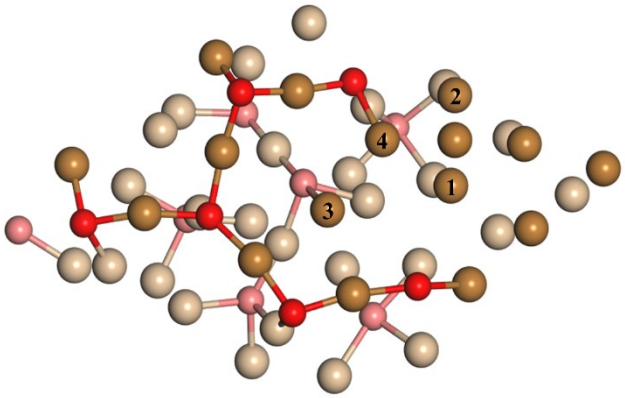

Figure S14. Schematic diagram for possible Sb doping sites on Cu/Cu_2O surface, and 1, 2, 3, and 4 sites refer to Cu/Cu_2O-Sb, Cu/Cu_2O-Sb2, Cu/Cu_2O-Sb3, and Cu/Cu_2O-Sb4 structures.

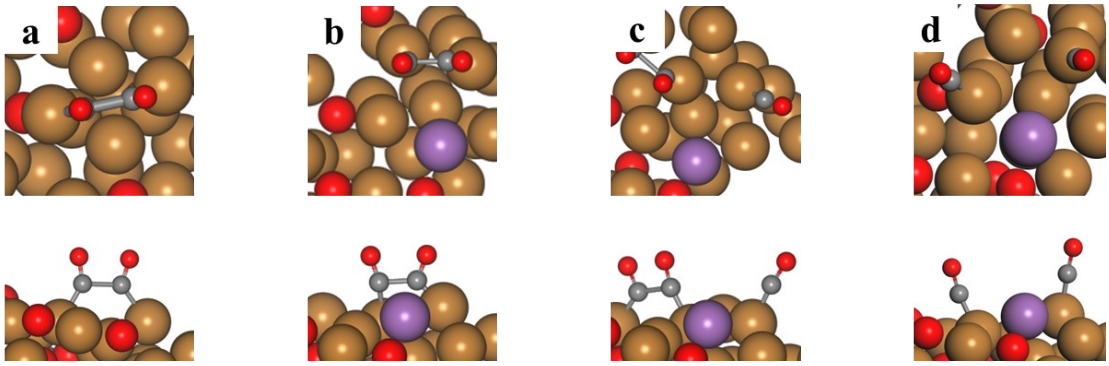

Figure S15. Optimized adsorption configurations of *OCCO intermediate on (a) Cu/Cu_2O, (b) Cu/Cu_2O-Sb, (c) Cu/Cu_2O-Sb-CO, respectively. (d) Optimized adsorption configuration of *CO on Cu/Cu_2O-Sb-CO.

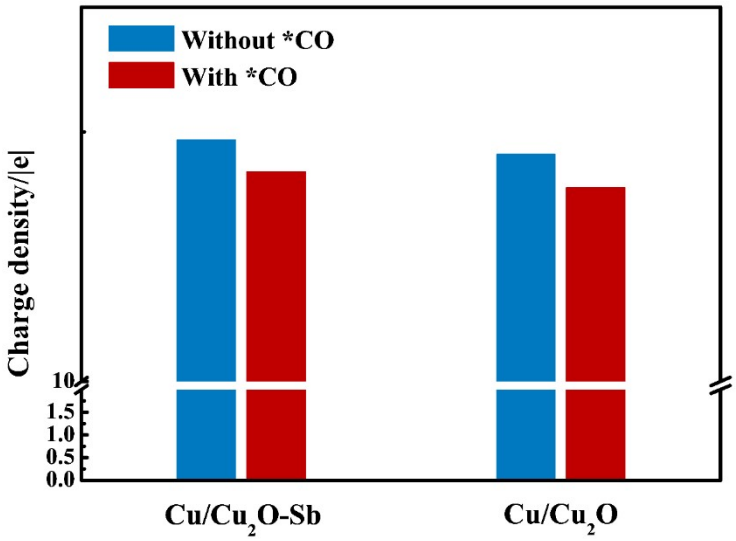

Figure S16. Bader charge of active site (Cu atom) before and after CO binding on Cu/Cu_2O-Sb and Cu/Cu_2O, respectively.

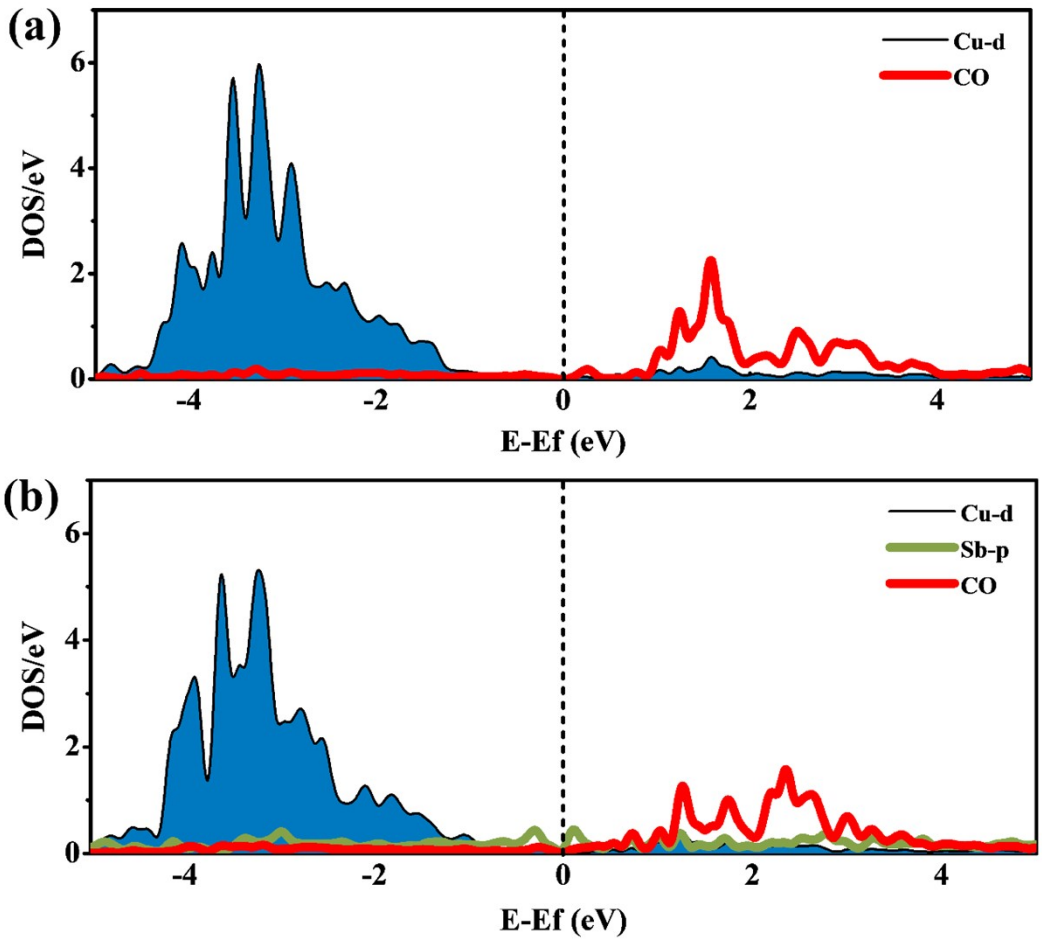

Figure S17. Density of orbital states (DOS) of CO binding on a. Cu/Cu_2O and Cu/Cu_2O-Sb, respectively.

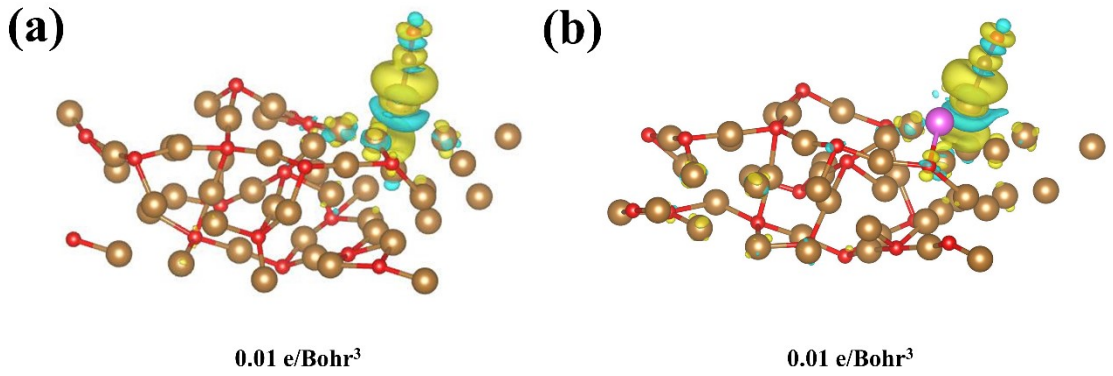

Figure S18. Electron density difference for CO binding on (a) Cu/Cu_2O, and (b) Cu/Cu_2O-Sb. Yellow is electron accumulation and cyan represents electron depletion.

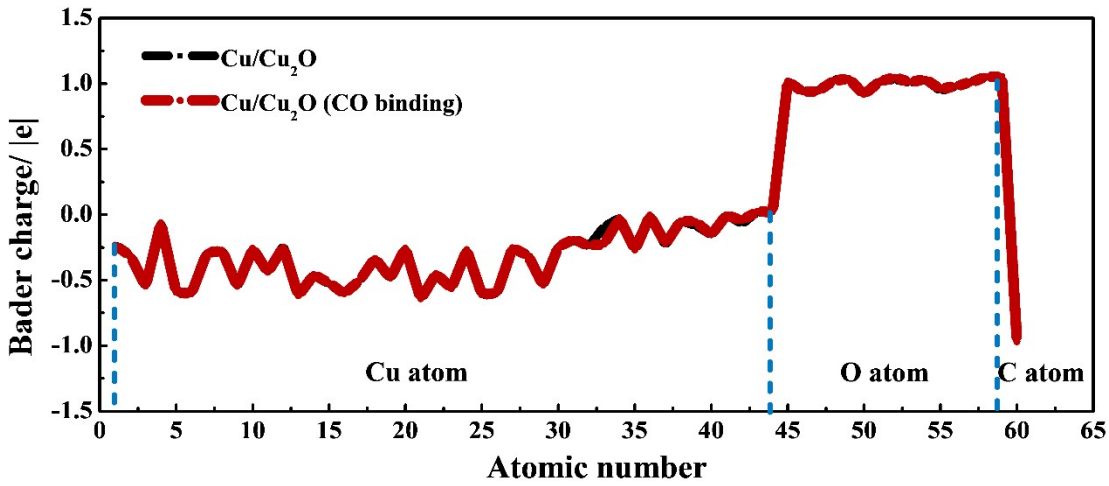

Figure S19. Bader charge tracking before and after CO binding on Cu/Cu_2O.

Table S1. Actual molar ratios of Sb/Cu and actual metal loadings on the catalysts measured by inductively coupled plasma optical emission spectroscopy (ICP-OES) analysis.

Catalysts	Cu wt.%	Sb wt.%	Sb/Cu molar ratio
Cu/Cu_2O-Sb-2.5	76.357	3.292	2.250%
Cu/Cu_2O-Sb-5	74.939	5.450	3.796%
Cu/Cu_2O-Sb-7.5	71.504	9.676	7.062%
Cu/Cu_2O-Sb-10	67.422	11.319	8.762%

Table S2. The double layer capacitance of different electrodes and the corresponding normalized roughness factor.

Electrodes	**C_{dl} (mF cm^{-2})**	**R_f**
Cu/Cu_2O	4.576	1
Cu/Cu_2O-Sb-5	10.283	2.25

Table S3. Summary of the reported Cu-based electrocatalysts for CO_2 electroreduction reaction to CO in the past two years.

Electrocatalysts	Potentials (V vs. RHE)	j_{CO} (mA cm^{-2})	FE (%)	Ref.
Cu/Cu_2O-Sb-5	-0.9	6.3	95	This work
Cu SAs/NC	-0.7	3.47	92	19
$NiCu_{0.25}$	-1.0	~0.5	88.5	20
CuFe/NC	-0.5	2.1	~93	21
Cu_5Pd_5	-0.87	4	88	22
Sn/Cu cones	-0.6	5.43	82.7	23
Sb-Cu	-1.1	~4.6	82	24
$Cu/In(OH)_3$	-1.0	10.1	89	25
$g\text{-}C_3N_4/Cu_2O$-FeO	-1.0	~3.75	84.4	26
Cu-Ni HF	-0.9V	10.54	77.5	27
CuO/Cu@BC	-0.6	~2.65	53	28
InCu	-0.8	~9.72	~87.6	29
Cu/Ag-3	-0.8	0.891	89.1	30
MR Cu Ms	-0.8	13.2	78	31
CuPolyPc@CNT	-0.7	5.6	80	32
Cu100nm-Ag3nm	-1.0	1.4	79.8	33

Table S4. Formation energy of Sb doped Cu/Cu_2O with different doping sites.

	Cu/Cu_2O-Sb1	Cu/Cu_2O-Sb2	Cu/Cu_2O-Sb3	Cu/Cu_2O-Sb4
Formation energy/eV	-0.94	-0.84	-0.81	-0.01

Table S5. Free energy changes for initial reduction of CO_2 to *CO intermediate and HER on Cu/Cu_2O and Cu/Cu_2O-Sb.

Elementary steps	ΔG/eV	
	Cu/Cu_2O	Cu/Cu_2O-Sb
Slab+CO_2+(H^++e^-)→*COOH	0.39	-0.81
*COOH+(H^++e^-)→*CO+H_2O	-0.66	-0.79
H^++e^-→*H	0.14	0.25

Reference

1 G. Kresse, J. Furthmüller, *Phys. Rev. B.* 1996, **54**, 11169-11186.

2 J. P. Perdew, K. Burke, M. Ernzerhof, *Phys. Rev. Lett.* 1996, **77**, 3865-3868.

3 K. Mathew, R. Sundararaman, K. Letchworth-Weaver, T. A. Arias, R. G. Hennig, *J. Chem. Phys.* 2014, **140**, 084106.

4 J. K. Nørskov, J. Rossmeisl, A. Logadottir, L. Lindqvist, J. R. Kitchin, T. Bligaard, H. J. Jo´nsson, *Phys. Chem. B.* 2004, **108**, 17886-17892.

5 Y. Hori, A. Murata, R. Takahashi, *J. Chem. Soc., Faraday Trans. 1*, 1989, **85**, 2309-2326.

6 Y. Mun, S. Lee, A. Cho, S. Kim, J. W. Han, J. Lee, *Appl. Catal. B-Environ.* 2019, **246**, 82-88.

7 W. J. Dong, C. J. Yoo, J. W. Lim, J. Y. Park, K. Kim, S. Kim, D. Lee, J-L. Lee, *Nano Energy* 2020, **78**, 105168.

8 M. Li, J. Wang, P. Li, K. Chang, C. Li, T. Wang, B. Jiang, H. Zhang, H. Liu, Y. Yamauchi, N. Umezawa, J. Ye, *J. Mater. Chem. A.* 2016, **4**, 4776-4782.